

Analysis and optimization of the reliable hole detection in sheet pile walls

Christian GAUS^{1,*}, Berit JOST¹, Timo PIERT¹, Christian HESSE², Karsten HOLSTE², and
Heiner KUHLMANN¹

¹ University of Bonn, Nussallee 17, 53115 Bonn, Germany, (gaus@igg.uni-bonn.de, jost@igg.uni-bonn.de, s7tipier@uni-bonn.de, heiner.kuhlmann@uni-bonn.de)

² HydroMapper GmbH, Veritaskai 8, 21079 Hamburg, Germany (ch@dhipi.com, Karsten.Holste@wk-consult.com)

*corresponding author

Abstract

At German ports and waterways, there are approximately 3,000 km of shoreline walls and about 2,500 km of traffic structures. As these structures have mostly reached an advanced age, it is essential to know whether they are still load-bearing. Therefore, these structures must be examined for their reliability. The common method to carry out this examination has been to deploy divers to inspect the walls underwater. This is very time-consuming, especially given that underwater light conditions in German ports are often poor. To overcome these disadvantages, sheet pile walls can also be surveyed using a multi-sensor system with a Multi-Beam Echo Sounder (MBES). This system measures the walls under water using sound waves and provides a point cloud of the structure. In the subsequent investigation, holes represent a particular interesting type of damage. However, so far, no statement could be made about the reliability of detecting these using sonar. To evaluate in how far the system is capable to detect holes in sheet pile walls, test samples with different geometric shapes, surface materials, and holes varying in size and shape are constructed. Knowing the geometry as well as the location and size of the holes, the reliability of the hole detection is investigated, considering especially the noise and resolution capability of the MBES. Furthermore, different measurement settings, such as pulse length and pulse power are analyzed for the best settings to be used for the hole detection.

Keywords: Damage detection, Multi-beam echo sounders, Sheet pile walls, Quality analysis

1 Introduction

Rivers and canals fulfill essential functions beyond transportation, including water supply, regulated drainage, flood control, and energy generation (Generaldirektion Wasserstraßen und Schifffahrt). Steel sheet piles are critical for stabilizing the shores and retaining soil. However, their lifespan is limited by factors such as corrosion, mechanical impacts, and ice pressure (Bundesanstalt für Wasserbau, 2017). Perforations are particularly severe, leading to soil erosion, ground subsidence, or structural collapse, threatening infrastructure safety. Germany's aging waterway infrastructure, with more than 3,000 km of shore walls nearing the end of their 80 to 100-year lifespan, underscores the urgent need for effective condition monitoring (Hesse et al., 2021). Modern multisensor systems, such as the one developed by the HydroMap-

per GmbH, combine laser scanning for above-water analysis and sonar technology for underwater inspection. While laser scanning is well-established, reliable sonar-based detection of holes in sheet piles remains a challenge.

To address this challenge, two specialized test walls were developed, featuring different geometries, surface textures, and artificially introduced holes of varying sizes and shapes. These test walls serve as controlled environments for evaluating different sonar parameters and configurations in detecting holes in steel sheet pile walls. Sonar data was collected from the walls to generate point clouds, which were then analyzed to identify potential holes. The study presents an automated process that includes outlier removal, modeling, and hole detection to analyze the influence of different measurement configurations and parameters on the hole

detection reliability.

In the following, we give an overview of the related work (section 2) and the measured data (section 3). Afterward, we present the methods (section 4) and analyze the results (section 5). Finally, we give our conclusion (section 7).

2 Related work

Kinematic multisensor systems represent a cornerstone of modern data acquisition technologies, enabling the precise capture of spatially resolved information about the surrounding environment. These systems rely on the integration of relative sensors, such as Inertial Measurement Units (IMUs), and absolute sensors, such as Global Navigation Satellite System (GNSS) antennas, to determine the position and orientation of the measurement platform with high accuracy (Kuhlmann and Klingbeil, 2017). Relative sensors provide information on changes in distance and rotation based on initial conditions, while absolute sensors deliver global positional data. Combining these sensor types through advanced fusion techniques, such as Kalman filtering, ensures robust and reliable trajectory determination, even in challenging environments.

Building on this foundation, sonar systems function by emitting acoustic signals that propagate through water and reflect off surfaces, returning as echoes to the system's receivers (Ferreira et al., 2022; Bjørnø and Buckingham, 2017). By analyzing the travel time of these signals and utilizing the speed of sound in water, the distance to the reflecting surface can be accurately calculated. Multi-Beam Echo Sounders (MBESs) expand on this principle by deploying a fan-shaped array of acoustic beams, enabling the simultaneous collection of multiple data points. This approach generates detailed 3D representations of underwater structures, such as the seabed, with significantly improved efficiency and spatial resolution compared to single-beam systems.

Key factors influencing data quality, including frequency, pulse length, and pulse power, must be carefully balanced to optimize resolution and range (Teledyne RESON, 2015). For instance, higher frequencies provide better resolution, capturing finer details of the underwater environment, but their range is limited due to greater attenuation (Bjørnø and Buckingham, 2017). In contrast, lower fre-

quencies penetrate farther, but produce less detailed measurements. Other critical parameters include pulse length, which affects axial resolution, and pulse power, which determines the system's effective range.

Environmental challenges, such as scattering, absorption, and noise, further complicate data acquisition (Abraham, 2019). These factors, combined with surface textures and angles of incidence, require meticulous adjustments to system configurations. To mitigate these challenges, careful adjustments to system parameters and configuration are essential to ensure accurate and consistent data acquisition under varying underwater conditions.

3 Data

This chapter outlines the test walls and the associated data collection process. The HydroMapper GmbH prepared two test walls for the study, differing in geometric dimensions and opening angles (50° and 65°). Each test wall was coated with three surface textures: fine (0 - 0.4 mm), medium (1 - 2 mm), and coarse (3 - 5 mm). Artificial holes of various sizes (small, medium, large) and shapes (square, triangular, rectangular, circular) were incorporated into designated areas of the walls (fig. 1).

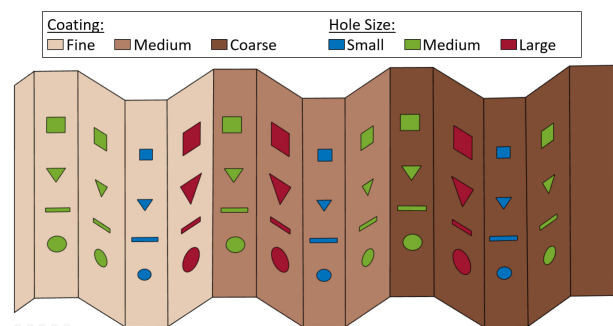


Figure 1. Model of the TLS point cloud (50° testwall).

The test walls were initially digitized using TLS to create reference models and document hole dimensions. Subsequently, they were submerged at the Hamburg-Harburg harbor for underwater measurements. The TLS-derived point clouds provided the basis for reference modeling and hole size validation.

Data collection was performed using a mobile multisensor system developed by the HydroMapper

GmbH. This system integrated an IMU with accelerometers, a gyroscope, and two GNSS antennas for precise positioning (Hesse et al., 2021). Measurements were carried out using the SeaBat T50-P MBES under various configurations (Teledyne Marine).

All measurements were conducted at a constant speed of 1.5 km/h. The MBES was fixed at a depth of 1.5 m and oriented with a vertical inclination of 30°. These parameters remained consistent throughout all measurements. In contrast, the following parameters were systematically varied: the pulse power (190kHz, 200kHz, 210kHz, 220kHz), scan mode (continuous wave (CW), frequency modulation (FM)), distance to the walls (5m, 8m), number of beams (512, 1024), pulse length (300μs, 30μs), coverage angle (focused on the test walls or focused on the wall + ground), and tracker mode (on, off). In addition, the horizontal angle between the wall and the MBES was changed using 5 different options (0°, ±15° & ±45°, e.g. fig. 2), which is in the following referred to as the measurement angle.

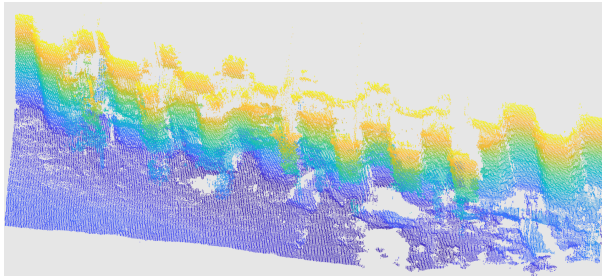


Figure 2. Example of a measured MBES point cloud

Various combinations of hole sizes, coatings, and wall angles were analyzed (table 1). For each combination, a square, a triangular, a rectangular, and a circular hole exist.

Table 1. Overview over measured holes

(a) Small				(b) Medium				(c) Big			
	Fine	Medium	Coarse		Fine	Medium	Coarse		Fine	Medium	Coarse
0°	2	2	2	0°	2	3	1	0°	-	-	-
50°	-	-	-	50°	1	1	1	50°	1	1	1
65°	-	-	1	65°	1	-	1	65°	1	1	1

4 Methods

In this section, the methodology for hole detection and the evaluation of various measurement configurations regarding hole detection is described. Since detecting holes in a two-dimensional space is more straightforward, the point cloud is transformed from 3D to 2D. Thereafter, a raster-based approach is employed for hole detection in 2D. To assess the detected holes — i.e., to determine whether they are genuine — a ground truth dataset is required. Based on the ground truth and the detected holes, a confusion matrix is set up and the *Youden – Index* is computed to evaluate the hole detection.

Following this, this section begins with an explanation of the reference model (section 4.1), which serves as a crucial basis for the transformation to 2D and the subsequent comparisons. Afterwards, the pre-processing of the MBES data is described (section 4.2), addressing the handling of outliers and preparing the data for evaluation. Finally, the hole detection process (section 4.3) and the evaluation methodology (section 4.4), is detailed.

4.1 Reference model

To determine which detected holes are true holes, a ground truth is needed. The ground truth is in this case established by constructing a model based on the TLS data. Fundamentally, the model consists of two sub-models: one representing the planar surfaces (M^S) and the other representing the holes (M^H). Together, these sub-models form the reference model M (fig. 1), i.e., the ground truth: $M = M^S \cup M^H$.

The model is composed of geodetic primitives, where M^S consists of planar surfaces, specifically planar rectangles, defined by the coordinates of their four corner points. Additionally, the holes M^H are also represented by geodetic primitives — specifically squares, triangles, rectangles, and circles, depending on their shape. These are likewise defined by their corner points and remain planar. An exception is made for circles, which, while also planar, lack distinct corner points and are therefore represented as point-based approximations.

4.2 MBES pre-processing

In this chapter, the preprocessing of the MBES point cloud is described. These steps are indispensable, given that MBES data exhibits a higher noise level than TLS data. Furthermore, the data is transformed from a three-dimensional model to a two-dimensional one. Thereby facilitating from a more straightforward analysis. This conversion is feasible without any loss of information, because the model only consists of planar planes.

Data preparation In this step, the MBES point clouds are cropped based on a bounding box and, if necessary, combined with other measurements. This point cloud is in the following referred to as P . Other measurements in this case mean other MBES measurements which were carried out at other measurement angles.

In addition to the cropping are outliers and excessive noise removed using a statistical method (Rusu et al., 2008). For each point p_i , the distances d_k to its k -nearest neighbors (k NNs) is calculated. If d_{ik} falls outside the range $\mu_d \pm \alpha \cdot \sigma_d$, the point p_i is identified as an outlier. Here, k and α are predefined parameters. The processed MBES point cloud is in the following referred to as P^C . This step is necessary to address the higher proportion of outliers in MBES data relative to TLS, thereby ensuring a better reference model fitting.

Fitting the reference The model M is aligned with the cleaned point cloud P^C using the least squares method. This involves determining the six transformation parameters (rotation and translation) through the Trust-Region Reflective algorithm (Coleman and Li, 1996). This algorithm operates by solving the optimization problem within a dynamically adjusted "trust region," which is iteratively refined to enhance convergence. The resulting optimal transformation is then applied to the model M .

Projection onto the model In this step, the cropped point cloud P is projected onto the reference surface model M^S to eliminate measurement noise. Since in this case a projection along the measuring line was chosen, the position of the sonar is required at each timestamp. This position is derived from the trajectory data. For each sonar point $p_S(t) \in P$ at time t , a corresponding trajectory point

$p_T(t)$ is determined via interpolation. A linear equation is then established between these points, and the intersection with the surface model is computed. To obtain a cleaner point cloud, points exceeding a distance of 10 cm from the model are identified and removed. The resulting cleaned intersection points constitute the projected point cloud P' , with each point assigned to the intersected surface i of the surface model M_i^S .

Rectified 2D projection To prepare for hole detection, which is carried out in 2D for reasons of complexity, both the model M and the point cloud P' are rectified and projected onto the xy -plane (fig. 3 (b)). Each surface i of the model undergoes an individual transformation consisting of the following three restriction steps:

1. **3D Rotation:** $n = [0, 0, 1]^T$
2. **Translation:** $M_i^S(1) = M_{i-1}^S(4)$
3. **2D Rotation:** $M_i^S(2) = M_{i-1}^S(3)$

Here, $M_i^S(k)$ represents the k -th vertex of the i -th surface. The transformation constraints for the first surface are set such that the first vertex aligns with the origin, and the second vertex intersects the negative y -axis.

After completing the projection, the rectified model and point cloud are referred to as \bar{M} and \bar{P} , respectively.

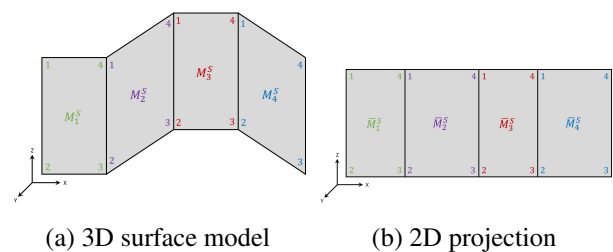


Figure 3. Representation of the 3D surface model and the 2D projection

4.3 Hole detection

To detect holes a raster and density based approach is used. Holes are thereby detected through identifying areas with significantly lower point density. The method examines each surface i individually, as point density varies due to differences in surface orientation. The chosen method was selected because, despite being undesired, points may appear

within the holes due to measurement noise and because to its capability to effectively manage these occurrences, this approach was selected.

First, a grid R_m , composed of m square cells with side length l , is overlaid on each model surface \bar{M}_i^S of \bar{M}^S . The side length l is calculated based on the point density of the points in \bar{P}_i . This is done in order to account for the varying point densities resulting from different incidence angles of the measurement beam.

To reduce noise effects within the grid, a mean filter utilizing a N_8 -neighborhood is applied. Finally, a threshold is determined to classify whether a grid cell represents a hole based on the number of points in the cell. The threshold is calculated using the Otsu method (Otsu, 1979), a non-parametric technique that performs discriminant analysis on gray-level histograms for automatic threshold detection.

4.4 Evaluation

As a result of the preceding steps, two key elements are obtained: a model M , serving as the ground truth, and a raster R_m that indicates for each cell whether it represents a hole or not. To derive a metric for classification performance, a confusion matrix is first constructed from this data. Subsequently, the selected evaluation metric is presented, along with the rationale for its choice. Finally the evaluation approach is described.

Confusion matrix To classify each grid cell from the hole detection process into the elements of a confusion matrix, it is essential to ascertain whether the cell truly represents a hole. For this purpose, a ground truth raster is constructed using the models. This raster is generated by intersecting the grid R_m with the hole polygons M_i^H . Grid cells overlapping more than 50% with a hole polygon are classified as holes.

Evaluation metric To evaluate the classification algorithm, standardized metrics are employed to assess the performance across different measurement configurations. The algorithm itself remains unchanged, ensuring that the evaluation exclusively reflects the influence of the measurement configuration.

Since the primary objective is to detect all holes, pri-

oritizing completeness over minimizing false positives, *Sensitivity* is chosen as an important evaluation metric. But due to significant measurement gaps in many configurations, *Sensitivity* values can be near 1, even when a hole can't realistically be detected. Therefore, *Specificity* was chosen as a second parameter to account for this case. In order to only have to handle one value at the end, the *Youden – Index* was chosen as the final evaluation metric. The *Youden – Index* is used, as it incorporates both the *Sensitivity* and *Specificity* for a more balanced evaluation ($\text{Youden – Index} = \text{Sensitivity} + \text{Specificity} - 1$).

Furthermore, the *Youden – Index* is set to 0 if the raster cells are too large to accurately detect holes, thereby eliminating unrealistic outcomes.

Evaluation approach At this stage, the analysis could begin by comparing the obtained values. However, since these values are subject to random variations, it is more appropriate to assess their statistical significance. For this purpose, it is beneficial to have multiple values per measurement configuration. Therefore, the adjusted *Youden – Index* is calculated for each plane M_i of the two models (50° and 65°). The values of one measurement configuration are then statistically compared to the distribution of another configuration, yielding in a *p – value*, which serves as the basis for further analyses.

To determine statistical significance, a significance level of 0.05 is applied. *P – values* smaller than this threshold indicate a statistically significant difference between the measurement configurations. To identify the superior configuration, the mean *Youden – Indices* of both configurations are compared.

Additionally, to enable the comparison of individual holes, a separate *Youden – Index^H* is calculated for each hole. The calculation utilizes the true negatives (TP) and false positives (FN) values per hole to determine the *Sensitivity*. For the *Specificity*, the corresponding value of the plane i is used since the true positives (TN) and false negatives (FP) values can't be assigned to the holes.

5 Results

This section begins with the presentation of the test wall modeling result (section 5.1), followed by an

analysis of the measurement parameters or configuration on the result of the hold detection process. Initially, the measurement parameters for various hole sizes (section 5.2) is evaluated, and subsequently, the influence of different measurement configurations (section 5.3) is examined.

5.1 Reference model

The sizes of the holes were determined using the models and subsequently averaged, as summarized in table 2. For the rectangular holes, only a single uniform size was considered. The measurements correspond to either the side length or the diameter of the holes.

Since the rectangles are all of equal size with an average height of 2.94 cm, they were all assigned to the small-hole group.

Table 2. Average hole sizes [in cm]

Size	Square	Triangle	Circle	Rectangle [w x h]
Small	7.18	7.85	7.65	15.3 2.94
Medium	10.58	10.25	10.48	- -
Large	15.52	18.59	15.15	- -

5.2 Hole size

This subsection describes the comparisons conducted based on hole size. To analyze the measurement parameters and configurations on the result of the hole detection process for different hole sizes, different measurement parameters and configurations were tested separately (e.g. fig. 4). For the comparison, the holes were categorized into three groups based on their size and the previously introduced *Youden – Index^H* is used for the evaluation of the measurement parameters for different hole sizes.

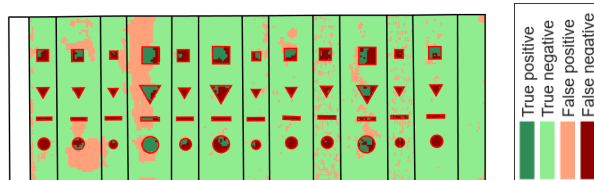


Figure 4. Resulting raster of the 50° test wall resulting from the combined measurements with 0° and ±15°

As no measurement configuration exhibited a normal distribution over all *Youden – Index^H* values of

the planes for all three groups (Shapiro-Wilk test), the Kruskal-Wallis and Mann-Whitney U-Test were applied for comparisons with a significance level of 0.05. A total of 30 individual measurements and 36 analyses combining multiple measurements (e.g. 0° combined with ±15°) were compared. In 42 cases (62.1%), small holes showed significantly worse results (*p – values* ranging from 0.000 to 0.04). In the remaining cases, 5 (7.6%) showed significantly better results for large holes (*p – values* ranging from 0.000 to 0.042 and from 0.459 to 1.000), 14 (21.2%) exhibited significant differences among all groups (*p – values* ranging from 0.000 to 0.025), and 4 (6.1%) revealed no significant differences (*p – values* ranging from 0.067 to 1.000). Additionally, in 2 cases (3%), no holes were detected. For this reason, subsequent analyses focus exclusively on medium and large holes.

5.3 Measurement configurations

This section compares the various measurement configurations. As no normal distribution is observed (Shapiro-Wilk test), the Wilcoxon- or Friedman-test with a significance level of 0.05 is used.

Overall, the mean *Youden – Index* of the measurements ranges from 0.00 and 0.29 (mean: 0.16, std: 0.08), indicating unsatisfactory detection performance across all measurements. However, these absolute values are ignored in the subsequent discussion, as only the relative differences are considered.

Pulse power The four pulse power settings (190 - 220 dB) are compared and no statistically significant differences is found (*p* = 0.257).

Scan mode and pulse length The comparison of scan modes inherently involves a comparison of pulse lengths, as FM was measured with 300 μs and CW with 30 μs. Similarly to the pulse power, no statistically significant differences is detected (*p – values* ranging from 0.078 to 0.658).

Distance No comparison is conducted regarding distance, since measurements performed at 8 m instead of 5 m did not detect any holes.

Number of beams A statistically significant difference is observed with respect to the number of beams (*p* = 0.001). Measurements with 1024

beams produced better results compared to those with 512 beams.

Coverage angle For this comparison, the coverage angle was set in two ways: one configuration captured the entire wall along with parts of the floor (approx. 90°), and the other focused on the test walls (approx. 30°). But no statistically significant differences is observed ($p = 0.600$).

Tracker mode The tracker mode adjusts the measurement settings based on previous measurements; consequently, a few meters of wall preceding the test wall were recorded. The tracker mode results in a statistically significant improvements compared to measurements without it ($p = 0.006$).

Measurement angle Finally, the influence of the measurement angle is analyzed. All possible angle combinations are aggregated and evaluated to determine the most suitable configurations. The comparison reveals several differences. Firstly, no significant improvement is observed when the same measurement is repeated (p – values between 0.439 and 0.886). With on exception with $\pm 15^\circ$ measurements, here is the usage of double measurements better (). Nonetheless this exception, these combinations are consolidated for the further analyses.

Table 3. Comparison of the different sensor angle positions (p-values)

	0°, ±15°	0°, ±45°	±15°, ±45°	0°	±15°	±45°
0°, ±15°, ±45°	0.129	0.174	0.201	0.030	0.729	0.000
0°, ±15°	-	0.047	0.109	0.000	0.003	0.000
0°, ±45°	-	-	0.343	0.144	0.535	0.000
±15°, ±45°	-	-	-	0.047	0.940	0.000
0°	-	-	-	-	0.029	0.201
±15°	-	-	-	-	-	0.005

Furthermore, measurements employing two angles (0° & $\pm 15^\circ$, $\pm 15^\circ$ & $\pm 45^\circ$, or 0° & $\pm 45^\circ$) are statistically neither better nor worse than those using three angles (0° & $\pm 15^\circ$ & $\pm 45^\circ$, with p – values between 0.129 and 0.201, table 3). Moreover, employing only one angle (0° or $\pm 45^\circ$) instead of two results in statistically significantly poorer performance (p – values between 0.000 and 0.047). One exceptions is noted: the comparison between the combination of 0° & $\pm 45^\circ$ with 0° showed no statistically significant differences ($p = 0.144$, table 3). However the combination with $\pm 15^\circ$ is statistically equal than other combinations with more than one

angle (p – values between 0.535 and 0.940), with the exception of 0° & $\pm 15^\circ$ ($p = 0.003$) where the later is the better one.

Lastly, in the comparison of the two-angle combinations, a statistically significant difference was observed only between combinations 0° & $\pm 15^\circ$ and 0° & $\pm 45^\circ$ ($p = 0.047$), with 0° & $\pm 15^\circ$ emerging as the superior option. No significant differences were noted among the other combinations (p – values between 0.109 and 0.343)table 3).

6 Discussion

This chapter briefly evaluates the experimental findings, focusing on how measurement configurations affect detection performance. It highlights the impact of parameters such as hole size, number of beams, tracker mode, and measurement angle, and explains how the sonar footprint limits the detection of small holes, thus directing attention to medium and large holes.

The inability to detect small holes was somewhat expected and can be explained by the sonar’s footprint. The footprint of the SeaBatT50-P is 1° (along-track) and 0.5° (across-track receiver) (Teledyne RESON, 2015). At a distance of 5 meters, 1° corresponds to 8.7cm. This already exceeds the size of the small holes. Consequently, subsequent analyses focus exclusively on medium and large holes. This rationale also explains why measurements at 8 m yielded no results. At this distance, the footprint is 14 cm (1°), exceeding the sizes of both small and medium holes and falling within the range of large holes.

Regarding the measurement angle, it was demonstrated that employing two angle settings (e.g. 0° and $\pm 15^\circ$) is sufficient for hole detection; additional angles do not further improve the results. Similarly, repeated acquisitions with the same setting do not yield better outcomes. For the two test walls (50° and 65°), the combination of 0° and $\pm 15^\circ$ proved to be the optimal setting. In particular, the $\pm 15^\circ$ angle emerged as the most suitable, likely due to a trade-off between the incidence angle on vertical (0°) walls and that on the inclined walls (50° and 65°). A $\pm 45^\circ$ measurement angle may result in an excessive incidence on vertical surfaces, whereas a 0° measurement angle may be suboptimal for inclined walls.

Additionally, differences were observed with respect to the number of beams. Here a higher number of beams yields better results, possibly because a greater number of points produces a denser measurement output and a higher *Specificity*.

Regarding the pulse power, its influence appears negligible, possibly due to the relatively short target distance in sonar applications. Lower energy settings may already yield accurate results, indicating that higher power levels do not compromise wall detection.

A similar rationale may apply to the coverage angle. Notably, while the coverage angle does not significantly affect the results, the number of beams does. Here, the beam coverage can be utilized, which is calculated from the angular width per beam and the distance to the measurement object. This is likely because the beam resolution is compared at 0.98 cm versus 1.95 cm, whereas the resolution for the coverage angle is compared at 0.98 cm versus 0.26 cm. In this case, the critical resolution threshold is probably already met at 0.98 cm, which explains the absence of significant differences.

7 Conclusion and outlook

In this study, various measurement settings were compared using different test walls and hole sizes, with the evaluation centered on each setting's capability to detect holes. The findings indicate that not all settings produced statistically significant differences. Notably, power, scan mode, and coverage angle did not yield significant variations. In contrast, the other parameters examined - hole size, distance, number of beams, tracker mode, and measurement angle - demonstrated different results. One finding is for example that a shorter measurement distance leads to improved results. However, it remains uncertain whether a minimum distance threshold exists and, if so, what its value might be. Additionally, an increased number of beams enhanced performance. Finally, it is advisable to combine three measurements: one at 0° and one each at ±15°.

References

- Abraham, D. A. (2019). *Sonar Systems and the Sonar Equation*, pages 33–93. Springer International Publishing, Cham.
- Bjørnø, L. and Buckingham, M. (2017). Chapter 1 - general characteristics of the underwater environment. In Neighbors, T. H. and Bradley, D., editors, *Applied Underwater Acoustics*, pages 1–84. Elsevier.
- Bundesanstalt für Wasserbau (2017). Bawempfehlung spundwanddickenmessungen in häfen und an wasserstraßen: Grundlagen, planung, durchführung, auswertung und interpretation (esm).
- Coleman, T. F. and Li, Y. (1996). An interior trust region approach for nonlinear minimization subject to bounds. *SIAM Journal on Optimization*, 6(2):418–445.
- Ferreira, I. O., de Andrade, L. C., Teixeira, V. G., and Santos, F. C. M. (2022). State of art of bathymetric surveys. *Bulletin of Geodetic Sciences*, 28(1):e2022002.
- Generaldirektion Wasserstraßen und Schifffahrt (no year). Wasserstraßen. <https://www.gdws.wsv.bund.de/DE/wasserstrassen/wasserstrassen-node.html>. Accessed: 15.01.2025.
- Hesse, C., Holste, K., Neumann, I., Esser, R., and Geist, M. (2021). 3d hydromapper - ein innovatives messsystem für die erfassung, prüfung und das management von wasserinfrastrukturbauwerken. *zfv*, 146(4):259–265.
- Kuhlmann, H. and Klingbeil, L. (2017). *Mobile Multisensorsysteme*, pages 93–129. Springer Berlin Heidelberg, Berlin, Heidelberg.
- Otsu, N. (1979). A threshold selection method from gray-level histograms. *IEEE Transactions on Systems, Man, and Cybernetics*, 9(1):62–66.
- Rusu, R. B., Marton, Z. C., Blodow, N., Dolha, M., and Beetz, M. (2008). Towards 3d point cloud based object maps for household environments. *Robotics and Autonomous Systems*, 56(11):927–941.
- Teledyne Marine (no year). Homepage. <https://www.teledynemarine.com/en-us>. Accessed: 15.01.2025.
- Teledyne RESON (2015). Seabat t-series portable: Operator's manual: Seabat t20-p / t50-p high-resolution multibeam sonar system.